

## Tizian Bucher<sup>1</sup>

Advanced Manufacturing Laboratory,  
Department of Mechanical Engineering,  
Columbia University,  
New York, NY 10027  
e-mail: tb2430@columbia.edu

## Adelaide Young

Advanced Manufacturing Laboratory,  
Department of Mechanical Engineering,  
Columbia University,  
New York, NY 10027  
e-mail: agy2107@columbia.edu

## Min Zhang

Mem. ASME  
Laser Processing Research Center,  
School of Mechanical and  
Electrical Engineering,  
Soochow University,  
Suzhou 215021, Jiangsu, China  
e-mail: mzhang@aliyun.com

## Chang Jun Chen

Mem. ASME  
Laser Processing Research Center,  
School of Mechanical and  
Electrical Engineering,  
Soochow University,  
Suzhou 215021, Jiangsu, China  
e-mail: chjchen2001@aliyun.com

## Y. Lawrence Yao

Fellow ASME  
Advanced Manufacturing Laboratory,  
Department of Mechanical Engineering,  
Columbia University,  
New York, NY 10027  
e-mail: yly1@columbia.edu

# Thermally Induced Mechanical Response of Metal Foam During Laser Forming

*To date, metal foam products have rarely made it past the prototype stage. The reason is that few methods exist to manufacture metal foam into the shapes required in engineering applications. Laser forming is currently the only method with a high geometrical flexibility that is able to shape arbitrarily sized parts. However, the process is still poorly understood when used on metal foam, and many issues regarding the foam's mechanical response have not yet been addressed. In this study, the mechanical behavior of metal foam during laser forming was characterized by measuring its strain response via digital image correlation (DIC). The resulting data were used to verify whether the temperature gradient mechanism (TGM), well established in solid sheet metal forming, is valid for metal foam, as has always been assumed without experimental proof. Additionally, the behavior of metal foam at large bending angles was studied, and the impact of laser-induced imperfections on its mechanical performance was investigated. The mechanical response was numerically simulated using models with different levels of geometrical approximation. It was shown that bending is primarily caused by compression-induced shortening, achieved via cell crushing near the laser irradiated surface. Since this mechanism differs from the traditional TGM, where bending is caused by plastic compressive strains near the laser irradiated surface, a modified temperature gradient mechanism (MTGM) was proposed. The densification occurring in MTGM locally alters the material properties of the metal foam, limiting the maximum achievable bending angle, without significantly impacting its mechanical performance. [DOI: 10.1115/1.4038995]*

*Keywords:* laser forming, metal foam, mechanical response, digital image correlation, bending mechanism

## 1 Introduction

Since its introduction in the first half of the 20th century, metal foam has been the subject of countless research studies. Many researchers have demonstrated the great potential of the material due to its high strength-to-weight ratio and its outstanding noise and shock absorption capacity [1,2]. Its material properties have been studied in great detail [3,4], and numerous potential industrial applications have been identified [5,6].

Despite all these efforts, metal foam products have rarely made it past the prototype stage. The reason is that industrial applications often call for intricately shaped parts that are challenging to manufacture. Near-net-shape manufacturing methods for metal foam do exist, such as three-dimensional printing [7], as well as a powder metallurgy process [8]. The former, however, is a notoriously slow process, limited to small production volumes and part sizes. The latter, in turn, requires molds, limiting it to large production volumes and moderately sized parts.

Metal foam is normally manufactured in generic shapes, such as slabs or sheets, and subsequently bent to the required shape.

This approach is less costly, can be implemented on a much larger scale, and yields a more uniform density distribution. The challenge associated with this method is that metal foam is prohibitively difficult to bend due to the foam's high moment of area and bending stiffness. Conventional mechanical bending methods have shown no success to date. 3-point bending, for instance, generates high tensile stresses that exceed the foam failure strength and cause immediate failure [9]. Similarly, hydroforming was shown to cause excessive densification [10]. Therefore, an alternative bending method is needed that does not exert mechanical forces.

Laser forming has been investigated as an alternative bending method, since it is a noncontact method that does not require part-specific molds. The process is considered an economic option for low to mid production volumes because it can be used to form arbitrarily sized parts into a wide range of geometries without a mold. Laser forming has been studied extensively for sheet metal forming, and many aspects have been investigated, such as strain rate effects [11] and process synthesis considerations [12].

Within the last decade, several research groups have attempted laser forming of metal foam and reported positive results. Experiments have been conducted with open-cell foams [13], closed-cell foams [14], and closed-cell foams with outside skin [15], each case showing that bending angles up to 45 deg are feasible. The

<sup>1</sup>Corresponding author.

Manuscript received March 31, 2017; final manuscript received January 4, 2018; published online February 12, 2018. Assoc. Editor: Hongqiang Chen.

reported experimental work involves parametrical studies, in which bending angles have been measured for a range of different processing parameters, such as power, spot size, scan speed, and cooling methods. Moreover, the process has been studied for a range of metal foam properties, such as densities, pore sizes, and sheet thicknesses. Additionally, issues related to microstructure [16] and heat treatments [17] have been addressed, and some predictive capabilities have been developed [14,18,19].

From the aforementioned work, a rather complete picture emerges about the processing window that is required for metal foam laser forming, and some rudimentary numerical capabilities have been developed. However, the existing work has three essential shortcomings.

First, none of the previous studies have addressed the underlying bending mechanism in sufficient detail. So far, it has been assumed, without experimental proof, that the temperature gradient mechanism (TGM), identified by Vollertsen [20] for sheet metal laser forming, is always the governing bending mechanism in metal foam laser forming. While this assumption has been experimentally confirmed from a thermal standpoint [21], metal foam does not meet the requirements of TGM from a mechanical standpoint, as discussed in Sec. 2.

Second, previous studies have observed the existence of a maximum bending angle [13,15], but no comprehensive discussion of the reasons for the limiting behavior has been made. Also, the cited studies failed to address the impact of laser-induced imperfections, which occur during large-bending angle experiments, on the mechanical performance of the foam.

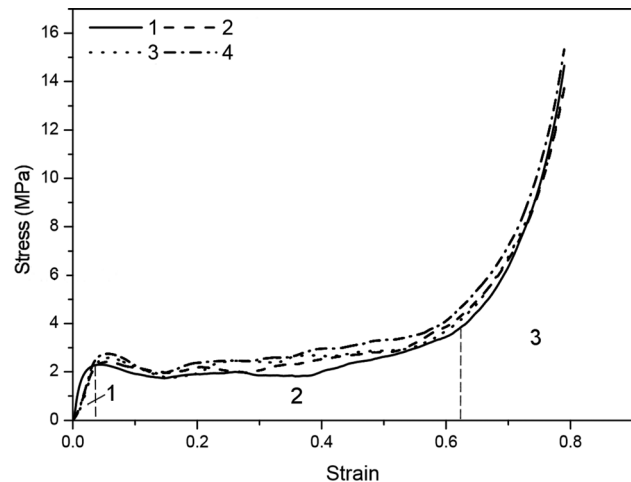
Finally, the cited experimental work is limited to bending angle measurements, and thus the existing numerical models have only been validated via the bending angle [14,19]. Additionally, the process has never been simulated up to large bending angles, and no comparison between models of different geometries has been done.

A step toward addressing the last issue was recently accomplished by measuring the transient temperature distributions in metal foam, using an infrared camera [21]. The obtained results were used to validate three numerical models with different levels of geometrical accuracy. In this study, the efforts from Ref. [21] were extended to the analysis of the mechanical aspects of laser forming. This was done by experimentally validating the numerical strain distributions using digital image correlation (DIC). Additionally, the bending mechanism was revisited by comparing metal foam laser forming with steel sheet laser forming, as well as 4-point bending. From the similarities and differences, a modified temperature gradient mechanism (MTGM) has been proposed. Finally, the limiting behavior of metal foam was investigated, both experimentally and numerically, by determining the extent of cell collapsing near the top surface, and monitoring the crack formation on the bottom surface. The impact of both of these imperfections on the foam crushability and structural integrity was investigated.

## 2 Background

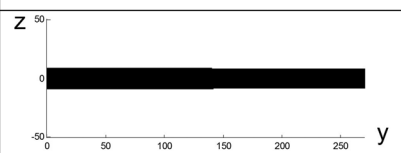
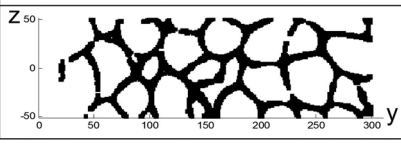
**2.1 Metal Foam Mechanics and Deformation.** Metal foam shows fundamentally different deformation behaviors in tension and compression. In tension, the material can undergo only a small amount of plastic deformation and has a low strength. In compression, on the other hand, the stress–strain curve can be divided into three distinct stages, as shown in Fig. 1. Initially, the stress increases linearly with strain, then transitions to a large “plateau” where cells collapse, followed by an exponential increase after the foam is fully compressed. Due to the wide plateau, the area under the stress–strain curve is large, explaining why metal foam is an excellent energy absorber.

Metal foam bending involves a combination of tensile and compressive deformation. Compared to solid material, metal foam has a very large bending stiffness  $S$ , which is defined as the resistance of the material to bending deformation and is denoted by



**Fig. 1 Uniaxial compressive stress–strain data (engineering) of four compression specimens (curves 1–4) made with the same metal foam that was used in this study [22]. The stress–strain curve can be divided into three segments: (1) a linear regime, followed by (2) a plateau where cell crushing occurs and a large amount of energy is absorbed, followed by (3) foam densification. Due to their crushability, metal foams can withstand much lower compressive stresses than solid metals.**

**Table 1 The moment of area (about  $z=0$ ) of a metal foam with 89% porosity is 43.4 times higher than the area moment of a solid with the same cross-sectional area. As a consequence, metal foam has a much higher bending stiffness.**

	Cross section	Moment of area
Solid		1
Foam		43.4

$$S = \frac{B_1 EI}{l^3} \quad (1)$$

where  $B_1$  is a scaling factor that is boundary and loading condition dependent,  $E$  is Young’s modulus,  $I$  is the moment of area, and  $l$  is the beam length [3]. The reason is that the moment of area of the foam is more than an order of magnitude greater than the moment of area of a solid with the same net cross-sectional area (Table 1), where  $I$  is calculated via

$$I = \int_{-s_0/2}^{s_0/2} z^2 y(z) dz \quad (2)$$

where  $s_0$  is the sheet thickness and  $y(z)$  the net section width at height  $z$ . Thus, the combination of high bending stiffness and low tensile strength explains why mechanical bending of metal foams is prohibitively difficult.

Unlike solid material, which is, in most cases, assumed to be incompressible, metal foam can yield due to deviatoric stresses as well as hydrostatic stresses. Assuming isotropic behavior, the

yield surface is a closed symmetric ellipsoid with aspect ratio  $\alpha$ , and the yield criterion involves both von Mises' equivalent stress  $\sigma_e$  and the mean stress  $\sigma_m$  [23]

$$F = \left[ \frac{1}{1 + (\alpha/3)^2} (\sigma_e^2 + \alpha^2 \sigma_m^2) \right]^{1/2} - Y \leq 0 \quad (3)$$

where  $Y$  is the uniaxial yield strength. When  $F < 0$ , the material behavior is elastic, and when  $F = 0$ , plastic deformation occurs pursuant to the following flow rule:

$$\dot{\epsilon}_{ij}^p = \frac{\dot{Y}}{H} \frac{\partial F}{\partial \sigma_{ij}} \quad (4)$$

where  $\dot{\epsilon}_{ij}^p$  is the plastic strain rate and  $H$  is the hardening modulus defined as

$$H = \frac{\sigma_e}{\hat{\sigma}} h_\sigma + \left( 1 - \frac{\sigma_e}{\hat{\sigma}} \right) h_p \quad (5)$$

where  $h_\sigma$  and  $h_p$  are the tangent moduli in uniaxial and hydrostatic compression, respectively, and  $\hat{\sigma}$  is the equivalent stress that is equal to the first term in the yield criterion (Eq. (3)).

**2.2 Bending Mechanism.** The thermo-mechanical bending mechanisms underlying laser forming are currently only well understood for solid materials [20]. For metal foam laser forming, it has thus far always been assumed, without experimental proof, that the TGM is the governing bending mechanism.

Temperature gradient mechanism was introduced by Vollertsen [20] for sheet metal laser forming, and it governs the scenario where a steep temperature gradient develops across the thickness of the workpiece. The material immediately below the laser spot heats up and tries to expand, but is restricted by the “cold” surrounding material. Instead of being able to expand, the material point becomes plastically compressed. This phenomenon occurs along the entire scan line, making the material shorter on the top surface and bending the workpiece toward the laser.

From a heat transfer standpoint, experiments have confirmed that steep temperature gradients develop across metal foam during laser forming [21], and thus the prerequisites for TGM are met. When investigating the mechanical aspects of laser forming, however, it becomes questionable whether TGM is valid for metal foam for several reasons.

First, the “shortening” that occurs in TGM via the formation of plastic compressive strain does not seem possible in metal foam, due to its crushability. The reason is that unless metal foam is in the densification stage, its yield strength is less than one 60th of the yield strength of the solid metal it is made of, since its fragile cell walls crush when subjected to large compressive stresses.

A second argument that puts TGM in question is the low tensile strength of metal foam. Even though TGM postulates that bending is mainly caused by compressive strains on the top surface, some tensile deformation occurs near the bottom surface as well. Solid metal can plastically deform in tension and thus accommodate the tensile deformation. Metal foam, on the other hand, can undergo only a small amount of plastic tensile deformation and fractures shortly beyond the linear elastic regime [24]. Thus, bending via TGM should cause an immediate fracture in metal foam. Hence, the traditional TGM does not fully capture the foam response during laser forming and needs to be revisited.

**2.3 Numerical Simulations.** The metal foam geometry was modeled using two different approaches shown in Fig. 2, with details explained in Ref. [21]. In the first model, “equivalent” model (used in Secs. 4.1–4.3), a solid geometry with equivalent foam properties, was used. In the second model, “Kelvin” model (used in Sec. 4.4), the foam geometry was modeled explicitly,

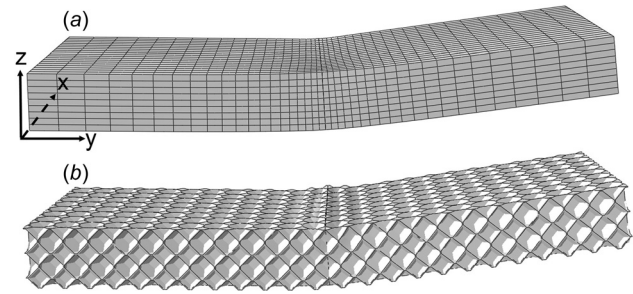


**Fig. 2** Two approaches were used to model metal foam. In the first (equivalent) model, shown in (a), a solid geometry was used and equivalent foam properties were assigned. In the second (Kelvin) model, shown in (b), the foam geometry was explicitly modeled, and solid aluminum properties were assigned. The cavity geometry was approximated by a Kelvin-cell geometry.

approximating the cavity geometry by a Kelvin-cell geometry, and assigning solid aluminum properties. The simulation was carried out using uncoupled thermo-mechanical analyses, whereby the output of the thermal analysis was used as a predefined field for the mechanical analysis. While this study exclusively discusses the mechanical aspects of the simulation, a detailed investigation of the thermal aspects may be found in Ref. [21].

In the equivalent model, the constitutive behavior was modeled using the equations introduced in Sec. 2.1, making two major assumptions: (1) the yield surface is symmetric, which has been verified for a similar metal foam [23], and (2) hardening occurs in an isotropic manner. The latter assumption is not valid for large deformations due to the fundamentally different responses of metal foam in tension and compression. Since the tensile strains are small compared to the compressive strains, the induced errors are small. In the Kelvin model, the constitutive behavior was modeled using von Mises' yield criterion and the Levy–Mises flow rule.

The foam's mechanical behavior at large bending angles was simulated using the equivalent model. The cell crushing behavior of the foam was modeled in an average sense, by calculating the volumetric plastic strain rate  $\dot{\epsilon}_m$  from the flow rule (Eq. (4)), using the expression [23]

$$\dot{\epsilon}_m \equiv \dot{\epsilon}_{ii}^p = \frac{\alpha^2 \dot{\hat{\epsilon}}}{[1 + (\alpha/3)^2]} \frac{\sigma_m}{\hat{\sigma}} \quad (6)$$

where  $\dot{\hat{\epsilon}}$  is the work conjugate strain rate of  $\hat{\sigma}$  that can be expressed as  $\dot{\hat{\epsilon}} = \dot{\hat{\sigma}}/H$ . The volumetric strain rate can also be written as  $\dot{\epsilon}_{ii} = \dot{R}/R$ , where  $R$  is the relative density and  $\dot{R}$  is the relative density variation rate. Integrating this equation gives the current relative density  $R$

$$R = R_0 \exp\left(-\int \dot{\epsilon}_{ii} dt\right) \cong R_0 \exp(-\Delta \epsilon_{ii}) \quad (7)$$

where  $R_0$  is the relative density at the previous time increment and  $\Delta \epsilon_{ii}$  are the logarithmic “true” strain increments in all directions [25]. Equation (7) was then used to calculate the relative density distributions at a cross section of the foam.

The simulations were implemented in ABAQUS, and densification calculations were performed in MATLAB. Multiscan simulations were performed on the Stampede supercomputer provided by Extreme Science and Engineering Discovery Environment [26]. Quadratic elements C3D20 were used for the equivalent model, and linear tetrahedral elements C3D4 were used for the Kelvin model. A  $y$ -symmetry boundary condition was used that set displacements in the  $y$ -direction (U2) and rotations about the  $x$ - and

$z$ -axes (UR1, UR3) equal to zero. Furthermore, the displacements in  $x$  and  $z$  (U1, U3) were restricted at two vertically aligned points on the symmetry surface. Rotations about the  $y$ -axis (UR2) were not restricted.

The thermal properties were used from Ref. [21]. The temperature-dependent thermal expansion coefficient  $\alpha_{th}(T)$  of the foam was assumed to be identical to that of the corresponding solid and was extracted from Ref. [27]. Temperature-dependent Young's modulus  $E(T)$  was obtained for solid AlSi11 [28] and converted to foam using relations given in Ref. [29]. The elastic and plastic Poisson's ratios  $\nu$  and  $\nu_p$  were obtained from Refs. [23] and [29], respectively. The flow stress  $\sigma_f$  was obtained from Ref. [22], and the temperature dependence was adapted from solid aluminum data [27]. The compressive yield stress ratio  $\sigma/p_c$  was estimated based on Ref. [23].

Steel sheet forming simulations were performed using the model in Ref. [11]. 4-point bending simulations were based on U-bend simulations developed by Brandal and Yao [30]. The loading block and supports were defined as rigid shells, and a general contact interaction, with zero friction, was used. Loading was exerted by vertically displacing the loading block.

### 3 Experimental Procedures

Closed-cell Al foam was used, with 7 wt % silicon, a volume fraction of 11.2%, and a density of  $279 \text{ kg/m}^3$ . The foam was manufactured employing a melt-foaming method that used  $\text{TiH}_2$  as a foaming agent and calcium to increase the viscosity of the liquid aluminum. Slitting cutters and end mill tools were used to cut test specimens to a length, width, and thickness of 100 mm, 35 mm, and 10 mm, respectively.

Laser forming experiments were performed using a continuous-wave Nd:YAG laser with a wavelength of 1064 nm. All the experiments were performed using a spot size of 12 mm, and the specimens were positioned below the focal plane to ensure that the laser intensity does not increase inside cavities (Fig. 3(a)). The specimens were clamped at one end using rubber pads to provide thermal insulation. Nitrogen was used as a protective gas to avoid oxidation, and in between successive scans, the specimen was allowed to cool to room temperature to prevent heat accumulation effects. The bending angle was determined by measuring the vertical deflection with a dial indicator.

The specimens were scanned underneath the laser using a six degrees-of-freedom Stäubli RX-130 robot. Two representative processing conditions were contrasted with (power, scan speed) of (90 W, 5 mm/s) and (180 W, 10 mm/s), respectively. The line

energy  $LE = P/v$  was kept constant, since constant LE experiments reveal several aspects of the physical behavior of metal foam and allow for a meaningful comparison with numerical simulations as has been shown in Ref. [31].

Digital image correlation was used to determine the strain distribution on the bottom specimen surface in between consecutive laser scans (Fig. 3(b)). The DIC experiments were performed by spray-painting the bottom specimen surfaces white and subsequently applying a black speckle pattern. A digital camera with a resolution of  $2448 \times 2048$  pixels was used to take images of the speckle pattern after each laser scan. To achieve the best resolution of about  $100 \mu\text{m}$ , it was ensured that the speckle sizes corresponded to 3–5 pixels on the digital camera [32,33]. The commercial DIC software VIC-2D from correlated solutions was used to calculate the Lagrangian strain fields from the digital images, which were subsequently converted to the logarithmic "true" strain fields. All the strains were computed in the tensile direction ( $\epsilon_{yy}$ ). Several calibration tests were performed to ensure that the results were independent of variables such as the subset, stepsize, seed placement, and incremental correlation. An example of a processed image is shown in Fig. 3(b), representing a strain distribution ( $\epsilon_{yy}$ ) at a bending angle of 45 deg.

To avoid strains induced by out-of-plane rotations [34], the strain was only extracted on the clamped half of the specimen above the bending axis (Fig. 3(b)). To minimize the impact of local inhomogeneities, the data were averaged over the entire specimen width and a distance of 5 mm from the bending axis. Standard errors were calculated over all individual pixels within that area.

The laser forming strain distributions were compared with strain distributions in 4-point bending experiments. 4-point bending tests were performed pursuant to a combination of ASTM standards D7249 and C1341. The data were averaged over a rectangle similar to laser forming, and was also corrected for strains caused by out-of-plane displacements [34].

### 4 Results and Discussion

**4.1 Bending Mechanism.** In Sec. 2, it was predicted that metal foam is unable to develop the compressive strains central to the traditional TGM, due to its crushability and low compressive strength. Laser forming experiments revealed two aspects of the foam behavior that spoke in favor of this prediction. First, no matter how low within the processing window the laser power was chosen, localized melting of thin cell walls was unavoidable. As

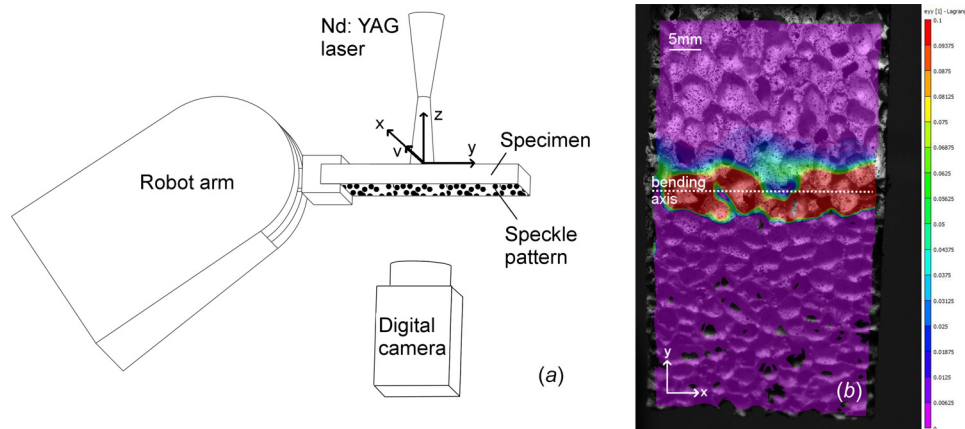


**Fig. 3** (a) Experimental setup. The laser was scanned in  $x$ -direction. The bottom specimen surface was spray-painted white with a black speckle pattern. Digital images were taken in between consecutive laser scans. (b) Example strain distribution ( $\epsilon_{yy}$ , Lagrangian strain) on the bottom surface of a laser formed specimen at a bending angle of 45 deg. The strain was only extracted on the clamped half of the specimen above the bending axis to avoid effects related to out-of-plane rotations [34].

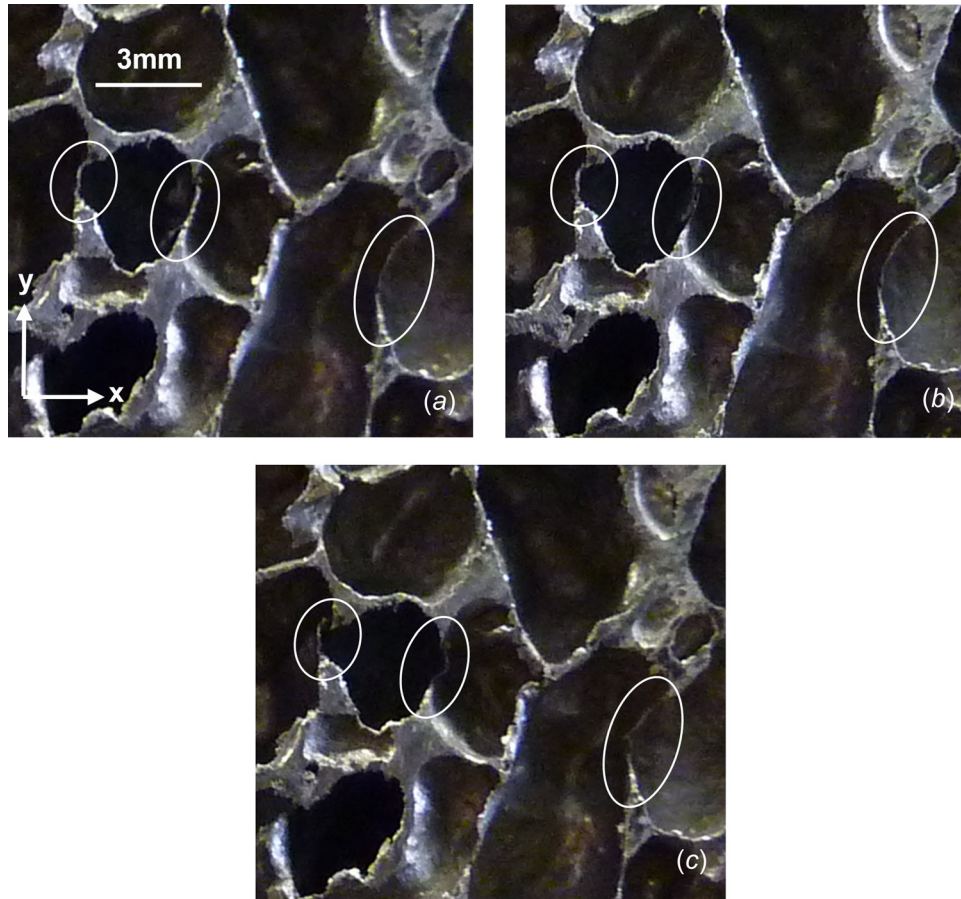


**Fig. 4** Section of the top surface of the specimen on the laser scan line (a) before laser forming, (b) after 1 scan, and (c) after 10 scans at 90 W and 5 mm/s. Even at this low power, localized melting of thin cell walls occurred, marked in white. Melting started after the first scan and progressed with each consecutive scan, forming u-shaped trenches in the cell walls and reducing the amount of compressible material. Melting stopped once the thickness of the remaining cell wall sections increased.

shown in Fig. 4, melting initiated at the first laser scan and progressed with each successive laser scan. Thin cell walls started melting from the top surface, forming u-shaped trenches that deepened until either the entire cell wall was melted away, or the cell wall thickness increased. If metal foam bending indeed occurred due to plastic compressive strains, melting would drastically impede bending, because it reduces the amount of compressible material. Experiments have shown the contrary, however, implying that plastic compressive strains cannot be the major cause of bending. The second aspect is that cell wall bending occurred close to the bending axis (Fig. 5), clearly indicating that the cell walls are unable to withstand high compressive stresses.

An alternative explanation is that metal foam bending is mainly caused by tensile stretching near the bottom surface instead of compressive deformation on the top. To investigate this hypothesis, the tensile strain  $\epsilon_{yy}$  (determined via DIC) was compared for laser forming and 4-point bending (Fig. 6).  $\epsilon_{yy}$  is the strain resulting from a combination of cell collapsing and cell wall deformation. In laser forming,  $\epsilon_{yy}$  indeed grew substantially larger than in 4-point bending, due to heat-induced softening. However, while the maximum  $\epsilon_{yy}$  in laser forming was around four times greater than in 4-point bending, the maximum bending angle was greater by a factor of 7. Therefore,  $\epsilon_{yy}$  did not grow proportionally to the bending angle; hence, tensile stretching cannot possibly account for all of the bending deformation.

Numerical results confirmed that tensile stretching is not the driving force of the bending deformation. Figure 7(d) shows the ratio of the compressive top surface strain to the tensile bottom



**Fig. 5** Cross section of a foam specimen after five laser scans at 180 W and 10 mm/s. The laser was scanned into the page. The white arrows show where cell walls were bent during laser forming, indicating that the foam cannot withstand high compressive stresses.

surface strain for metal foam laser forming, steel sheet laser forming, and 4-point bending (models shown in Figs. 7(a)–7(c)). The equivalent model was used for the simulation of metal foam, which was experimentally validated in Refs. [21] and [35]. In all cases, the strains were extracted at the bending axis. For foam and steel laser forming, the ratio was averaged over 10 scans and two typical conditions [foam—(90 W, 5 mm/s; 180 W, 10 mm/s), steel—(400 W, 25 mm/s; 800 W, 50 mm/s)], to obtain a most

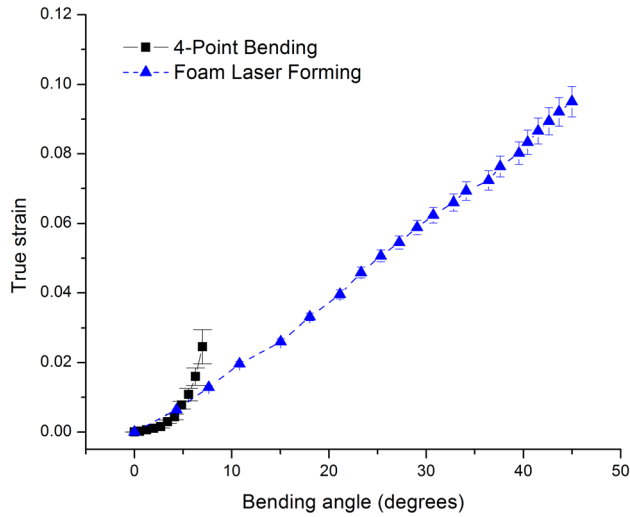


**Fig. 6** Comparison of the tensile strain ( $\epsilon_{yy}$ ) on the bottom surface (determined via DIC) in 4-point bending and laser forming (at 180 W and 10 mm/s).  $\epsilon_{yy}$  is the strain resulting from a combination of cell collapsing and cell wall deformation. Standard errors are shown, calculated over all the pixels of the averaged areas (see Sec. 3). In 4-point bending, the strain increased exponentially before a catastrophic failure, whereas in laser forming there was a stable linear strain growth with increasing bending angle. Laser forming yielded a larger maximum  $\epsilon_{yy}$ , due to heat-induced softening, yet  $\epsilon_{yy}$  did not grow proportionally to the bending angle, and hence tensile stretching cannot be the main cause of bending.

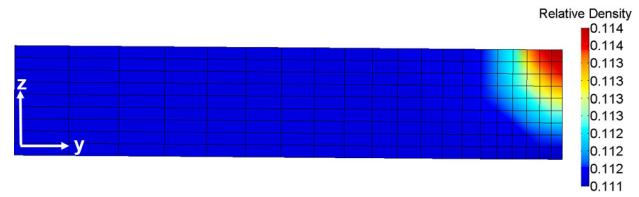


**Fig. 8** Relative density distribution after a single scan at 180 W and 10 mm/s. The baseline relative density is 0.112, and a relative density of 1 indicates complete densification. Densification occurred throughout the top 80% of the foam, leaving only a small tensile region on the bottom surface. Therefore, laser forming shifts the neutral axis downward, and deformation is dominated by compressive shortening.

representative value. For 4-point bending, the ratio was averaged over all the bending angles until the experimental failure angle. The results in Fig. 7(d) clearly show that; whereas compression and tension contributed equally in 4-point bending, compressive deformation was the major cause of bending in laser forming. Interestingly, metal foam and steel sheet laser forming nearly yielded the same ratio, implying that the compressive “shortening” on the top surface should be identical in both metal foam and steel.

Numerical relative density distributions at a cross section, calculated after a single laser scan at 180 W and 10 mm/s (Fig. 8), allow a similar conclusion to be drawn. The baseline relative density is 0.112, and a relative density of 1 indicates complete densification. The densified (compressed) region stretched over the top 80% of the foam, leaving only a small expanded (tensile) region on the bottom. Therefore, laser forming seems to shift down the

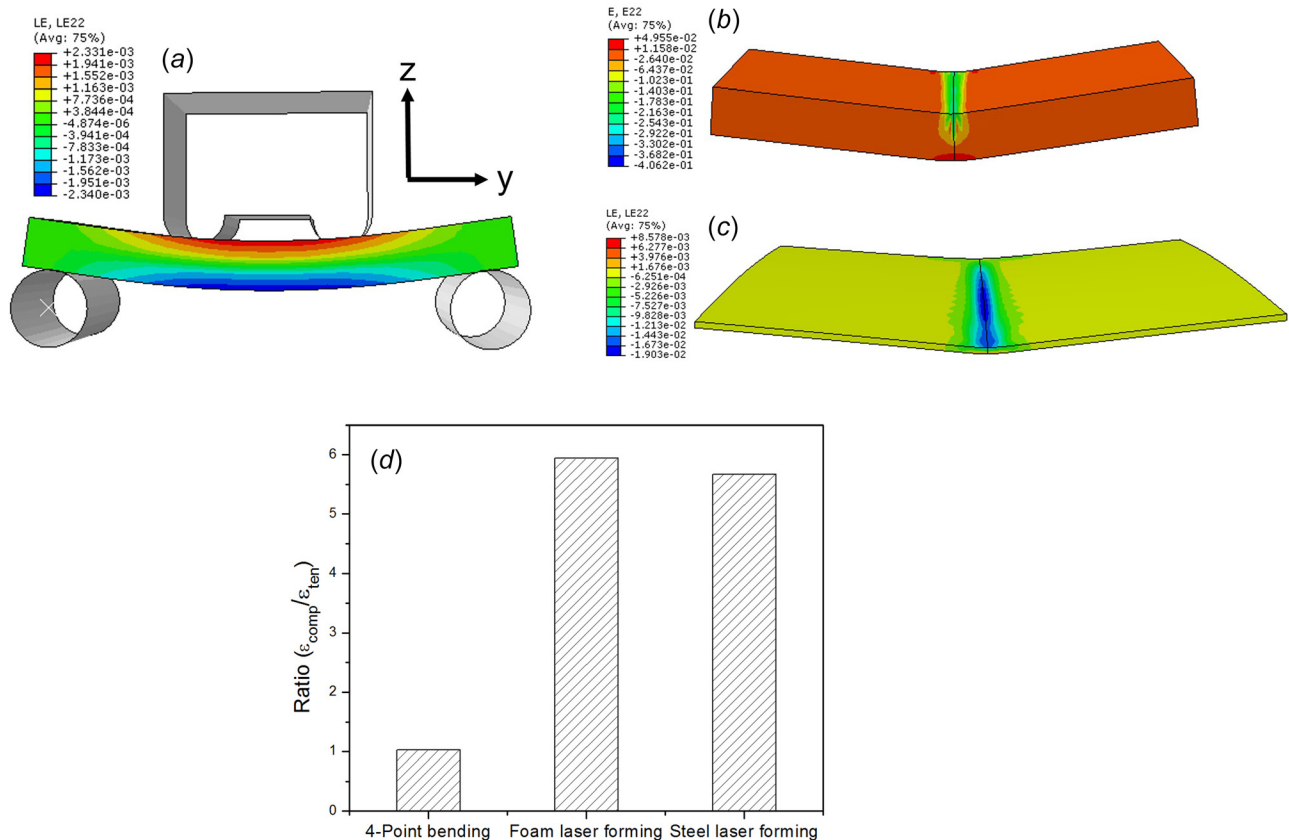


**Fig. 7** Strain distributions ( $\epsilon_{yy}$ ) in (a) metal foam during 4-point bending, (b) metal foam during laser forming, and (c) a steel sheet during laser forming. (d) Ratio of top surface (compressive) strain over bottom surface (tensile) strain at the bending axis, calculated for all three simulations. In 4-point bending, bending was equally caused by compressive and tensile strains. In laser forming, the large ratios indicate that compressive deformation was the main cause for bending.

neutral axis and limits the amount of tensile deformation occurring, unlike in 4-point bending (Fig. 7(a)), where the neutral axis lies midway through the thickness (assuming small bending angles).

The findings in Figs. 4–8 allow only one explanation: cell wall bending and cell crushing in metal foam laser forming, observed in Fig. 5, is equivalent to plastic compressive strains in steel sheet laser forming.

Using that insight, the bending mechanism of metal foam can be revisited. Metal foam develops steep temperature gradients across its thickness and thus meets the thermal prerequisites of TGM [21]. Similar to solid metal, bending is mainly achieved via compressive deformation, and tensile deformation near the bottom surface only occurs to accommodate the “shortening” on the top surface. The reason for its “shortening” near the top surface, however, differs from conventional TGM. Unlike solid sheet metal, which develops plastic compressive strains, metal foam shortens due to cell wall bending and cell collapsing. Moreover, metal foam does not immediately undergo a tensile fracture on the bottom surface due to heat-induced softening, as well as a downward shift in the neutral axis that limits the amount of tensile deformation. Since metal foam still meets most of the requirements set by TGM, this revised bending mechanism may be called MTGM.

**4.2 Bending Limit.** For laser forming of solid sheet metal, several studies reported that the bending increment decreases with increasing laser scans [36,37]. In laser forming of metal foam, a similar limiting behavior was observed at two different processing conditions, (high—180 W; 10 mm/s) and (low—90 W; 5 mm/s), shown in Fig. 9. In the experiment, as well as the simulation, the rate of change of both the bending angles and tensile strains decreased with an increasing number of scans and eventually approached zero, indicating that there is a maximum achievable bending angle.

In solid metals, the limiting behavior can be attributed to increases in the sheet thickness, strain hardening on the bottom surface, and variations in the laser absorption due to coating removal and heat-induced surface discoloration [36,37]. In metal foam, on the other hand, thickening does not occur, and neither does strain hardening on the top surface, since the flow stress remains constant until densification. Tensile strain hardening on the bottom surface only occurs to a small extent because metal foam can only undergo limited amounts of plastic tensile deformation. Variations in the laser absorption do occur in metal foams, since cavities crush and rotate with increasing bending angle, but they are not significant enough to be the major cause of the bending limit. Similarly, melting ceases after a few laser scans and cannot be responsible for the limit either.

Therefore, the bending limit must be caused by a phenomenon that does not occur in sheet metal laser forming, which is cell crushing and the subsequent densification. Densification increases the amount of material away from the central axis of the foam, and hence increases its moment of area, rendering the foam stiffer. Simultaneously, both Young’s modulus [29] and the flow stress [1] of the foam increase exponentially with its relative density, as shown in

$$\frac{E_f}{E_s} = \frac{(1 - \rho_f/\rho_s)^2}{(1 + (2 - 3\nu_s)\rho_f/\rho_s)} \quad (8)$$

$$\frac{\sigma_f}{\sigma_s} \approx 0.3 \left( \phi \frac{\rho_f}{\rho_s} \right)^{\frac{2}{3}} + (1 - \phi) \frac{\rho_f}{\rho_s} \quad (9)$$

where  $E_f$ ,  $\sigma_f$ , and  $\rho_f$  are the Young’s modulus, yield strength, and density of the foam, respectively, and  $E_s$ ,  $\sigma_s$ , and  $\rho_s$  are the corresponding solid properties.  $\nu_s$  is the Poisson’s ratio of the solid, and  $\phi$  is the percentage of solid material at cell intersections, which was assumed to linearly increase with foam density.

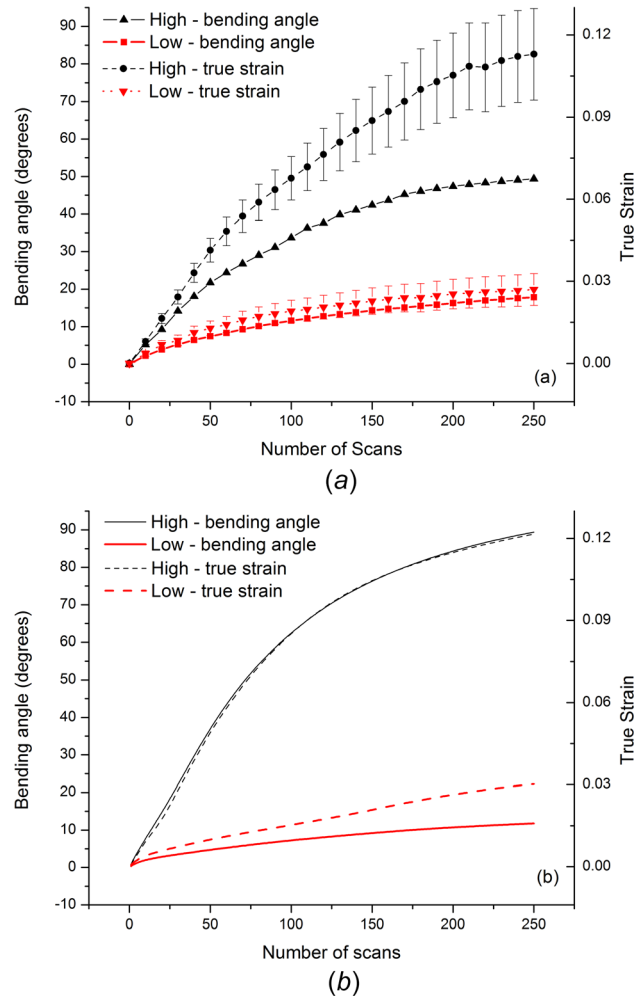


**Fig. 9 (a) Experimental and (b) numerical bending angles and tensile strain data ( $\epsilon_{yy}$ ) at large bending angles. “High” refers to the condition 180 W 10 mm/s, “low” refers to 90 W 5 mm/s. Standard errors are shown for the strain results, calculated over all the pixels of the averaged area (see Sec. 3). In both the experiment and the simulation, the bending angle and strain plots leveled off at a large number of scans. In the numerical simulation, the limit at 180 W and 10 mm/s was reached at a larger bending angle, since the model did not consider melting, as well as changes in the moment of area, laser absorption and thermal conductivity with increasing densification.**

These equations show that densification stiffens the foam even further and reduces the amount of plastic deformation. Densification also increases the thermal conductivity, as is shown by [3]

$$\left( \frac{\rho_f}{\rho_s} \right)^{1.8} < \frac{k_f}{k_s} < \left( \frac{\rho_f}{\rho_s} \right)^{1.65} \quad (10)$$

where  $k_f$  and  $k_s$  represent the foam and solid thermal conductivities, respectively. As a consequence, the heat diffusion away from the top surface increases, thereby reducing the amount of thermal expansion and plastic compressive deformation. Hence, densification is the main reason for the bending limit in metal foam laser forming.

From the results in Fig. 9, it is apparent that (180 W; 10 mm/s) yielded a higher maximum bending angle than (90 W; 5 mm/s). The reason is that, for an increased power and speed (at  $LE = \text{const.}$ ), heat has less time to dissipate, thus increasing the temperature rise, thermal expansion, and plastic compressive

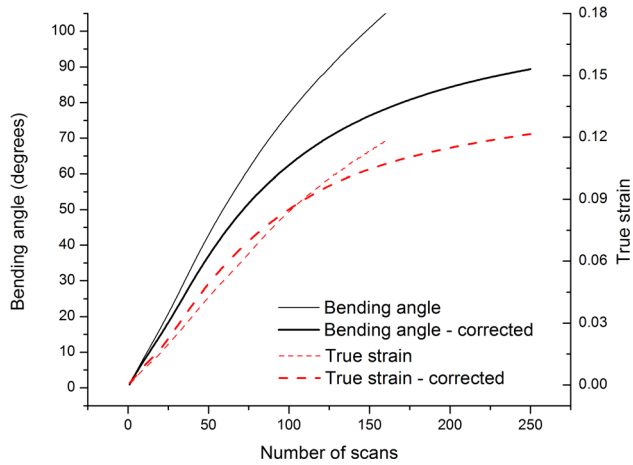


**Fig. 10 Comparison of numerical data before and after correcting for density dependence. Without correction, both the bending angle and strain increment decreased only slightly with increasing scans, induced by tensile strain hardening on the bottom surface. After incorporating density-dependent variables, a distinct limiting behavior could be observed.**

“shortening” close to the top surface [21,31]. Hence, more densification is required to stop the plastic compression from occurring.

Numerical results confirm the above reasoning. Without accounting for densification effects, the bending and strain increment only slightly decreased with increasing laser scans in Fig. 10, whereby the decrease was caused by tensile hardening on the bottom surface. When calculating the density as a field variable using  $\rho = \rho_0 e^{-(\epsilon_{ii})}$  (from Eq. (7)) and incorporating density-

dependent Young’s moduli and flow stresses from Eqs. (8) and (9), both the bending and strain increment decreased much more quickly, and the resulting corrected results agreed better with the experimental trends. Therefore, simulations confirmed that densification-induced changes in the material properties are the major cause of the bending limit.

While the numerical results agreed with the experimental results at 90 W and 5 mm/s, they overestimated the bending angle at 180 W and 10 mm/s, and simultaneously underestimated the tensile strain on the bottom surface. Several approximations in the model led to this error that only became significant at large bending angles and higher powers/speeds. First, melting was neglected, which relaxes stresses in the material and thus reduces the amount of bending. Second, the model failed to account for changes in the moment of area, owing to its solid geometry. Finally, since it is an uncoupled analysis, the model did not account for changes in the laser absorption, as well as densification-induced changes in the thermal conductivity,  $k$ , whose impact can become significant at large bending angles. This problem could be mediated by using a coupled thermo-mechanical analysis, but doing so currently renders the simulation too CPU-intensive to study laser forming at large bending angles.

#### 4.3 Impact of Laser Forming on Metal Foam Performance.

Bending deformation in metal foam laser forming is achieved by introducing irreversible plastic deformation, which, as was shown previously, manifests itself mainly through cell crushing and some tensile deformation. This plastic deformation may affect the performance of metal foam as a crash absorber and structural member. In this section, it is demonstrated that the impact of laser-induced imperfections is negligible until large bending angles are reached.

A first type of laser-induced imperfections is crack formation near the bottom surface. Some thin cell walls, which have

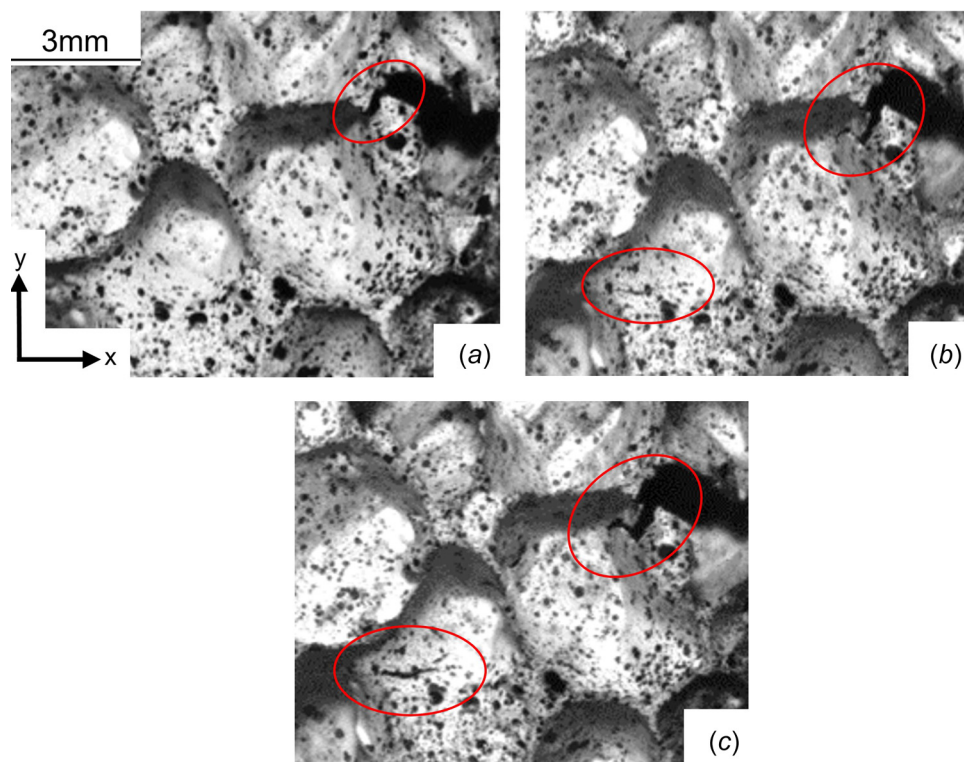


**Fig. 11 Bottom surface of a specimen scanned at 90 W and 5 mm/s at bending angles of (a) 1 deg, (b) 11.6 deg, and (c) 16.3 deg. Due to some naturally occurring stress concentrations, microcracks already occurred at low bending angles of 1 deg. As the bending angle became larger, those microcracks increased in size, and new microcracks formed ((b) and (c)). However, the microcracks remained isolated from each other at this stage and thus hardly affected the structural integrity of the foam.**

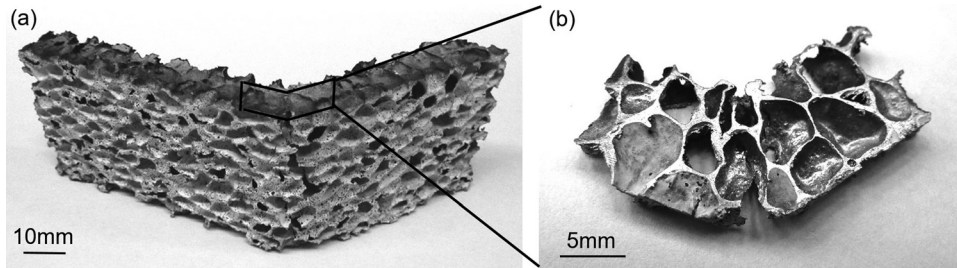


**Fig. 12** (a) Foam specimen at a bending angle of 45 deg, after being laser formed at 180 W and 10 mm/s, with a cross section shown in (b). At large bending angles, the isolated cracks on the bottom surface grew larger and started to coalesce, shown in (a). In close proximity to the bending axis, cells at the top surface were crushed significantly, shown in (b), but the foam was still far away from complete densification.

naturally occurring stress concentrations, while also being favorably aligned with the bending direction, can form microcracks already at low bending angles of 1 deg (Fig. 11(a)). More microcracks form with increasing bending angles (Figs. 11(b) and 11(c)), but they are small in size and remain isolated from each other. Once the bending angle approaches 45 deg, the cracks grow and start coalescing, forming a more visible crack (Fig. 12(a)).

The impact of those micro and macrocracks on the structural strength of metal foam can be determined by analyzing its fracture behavior. Sugimura et al. [38] and McCullough et al. [39] showed that metal foam does not fracture in a “clean” manner. Instead, the cellular structure makes crack propagation rather tortuous, and major cracks in the foam are always preceded, and accompanied by, small side cracks. Therefore, even in the presence of microcracks, metal foam is still far away from complete failure, unlike a typical brittle material, in which the smallest crack can initiate a catastrophic failure.

Further insight can be obtained by evaluating the  $J$ -value, which is defined as the decrease in potential energy due to the growth of an incremental crack length,  $\Delta a$  [40]. Figure 13 shows the  $J$ -integral resistance curve obtained by Sugimura et al. for a similar foam [38]; comparable results were obtained by McCullough et al. [39]. The exact crack length, up to which the  $J$ -integral resistance curve is reliable, depends on the precise specimen geometry, particularly the distance that is available for crack growth as per ASTM E813-89. Regardless of the geometry, however, the  $J$ -curve in Fig. 13 shows a clear tendency to increase with crack length, unlike for brittle materials, where the  $J$ -curve describes a horizontal line beyond an unstable crack length [41]. Therefore, the microcracks observed in Fig. 11 hardly reduce the crack resistance, and even large cracks do not entirely remove the structural integrity of the foam.

While the aforementioned fracture analysis applies to mechanically fractured aluminum foam, it can be shown that the fracture behavior of laser-formed metal foam is even less of concern. Figure 14 shows a comparison between the fracture surfaces in 4-point bending and laser forming. Whereas the fracture surface in 4-point bending contained a mix of rough ductile dimples and clean brittle surfaces with sharp edges, the material on the laser formed fracture surface appears to have been pulled toward the right side, and thus has undergone a substantial amount of plastic deformation before fracture. Hence, the fracture in laser forming was much more ductile, due to a heat-induced reduction of the flow stress, which explains why laser forming yielded much larger tensile strains  $\epsilon_{yy}$  in Fig. 6. This result further emphasizes that the structural integrity of laser formed metal foam, even more so than untreated foam (in Fig. 13), is hardly affected by microcracks until large bending angles are reached.

The second type of imperfection introduced by laser forming is cell crushing, first discussed in Fig. 5, and now shown intensified at a large bending angle in Fig. 12(b). In order to determine the impact of cell crushing on the foam crushability, the changes in

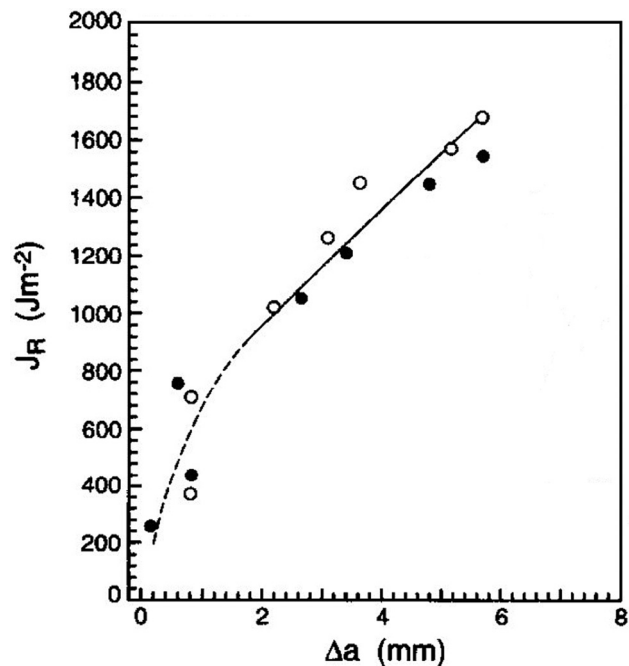


**Fig. 13** Resistance curves determined using the  $J$ -integral method, ASTM 813-89, for a closed-cell foam with a very similar composition and porosity [38]. The white and black data points represent two test specimens. Unlike in a brittle material, where the  $J_R$ -value would be horizontal beyond an unstable crack length, it keeps on increasing in metal foam, indicating that the foam fracture toughness is maintained even as the crack grows larger. Therefore, microcracks do not lead to an unstable fracture, and even larger cracks do not completely remove the structural integrity of the foam.

the relative density at large bending angles were analyzed, shown in Fig. 15. Even at a bending angle of 45 deg, the maximum relative density achieved was 0.271, which is far away from complete densification of  $R=1$ . Figure 15 further shows that the compressed area is highly localized around the bending axis, which is also the case in the experiment (Fig. 12(b)). Therefore, while cell crushing does to an extent reduce the compressibility of metal foam, it occurs in a highly localized manner, and to a degree that does not severely hamper the performance of metal foam as a crash absorber.

**4.4 Alternative Numerical Models.** So far, the numerical simulations were performed using a solid geometry model, which was found to induce errors due to its inaccurate laser absorption [21], as well as its inability to model changes in the moment of

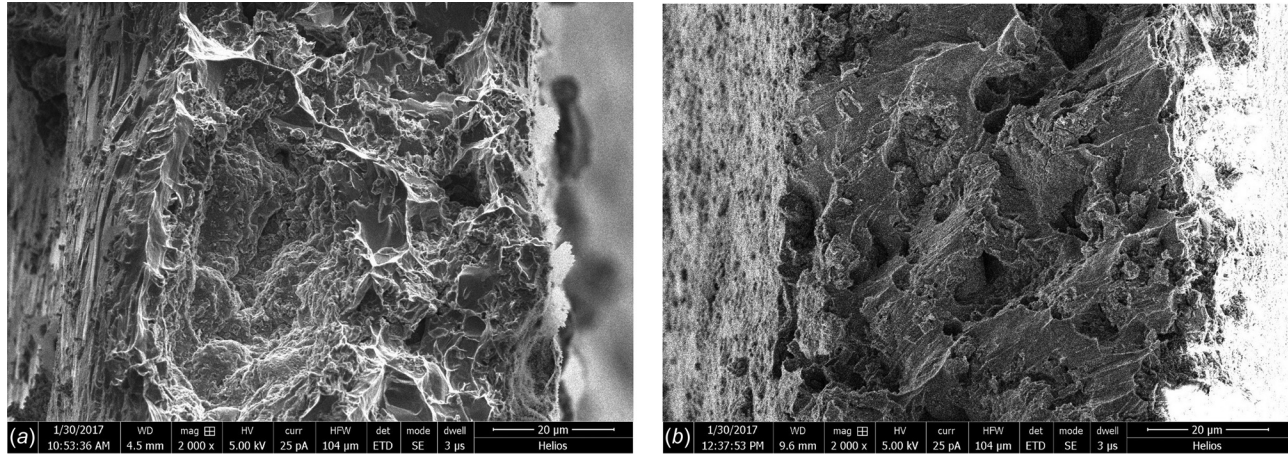


Fig. 14 Fracture surfaces in (a) mechanically fractured and (b) laser formed metal foam specimens. The fracture surface in (a) consists of a mix of dimples and clean surfaces with sharp edges, indicating a mix of ductile and brittle fracture. The material on the surface of (b), on the other hand, appears to have been stretched severely, indicating a more ductile fracture.

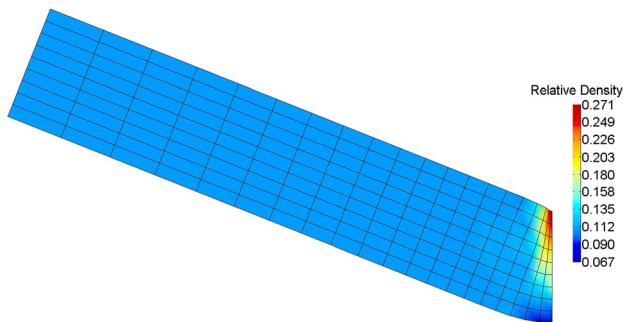


Fig. 15 Relative density distribution at a bending angle of 45 deg. The baseline relative density is 0.112, and a relative density of 1 indicates complete densification. The densified region was highly localized around the bending axis. Over a small area close to the top surface, the relative density increased by a factor of 2.5, which is still far away from complete densification. Foam expansion occurred close to the bottom surface, coinciding with the region where cracks appeared in Fig. 12(a).

area with increasing bending angle. These issues can be remedied by explicitly modeling the foam geometry.

Figure 16 shows the bending angle predictions of a Kelvin model for 8 laser scans, in comparison with the equivalent model predictions and the experimental data. The high and low conditions again refer to (180 W; 10 mm/s) and (90 W; 5 mm/s), respectively. On the one hand, the Kelvin model yielded results that more closely matched with the experimental values, due to its improved geometrical accuracy. On the other hand, the model still overestimated the bending angle at 180 W and 10 mm/s, since it did not account for melting, as well as changes in the laser absorption with increasing bending angle (due to using an uncoupled analysis). Also, the model geometry was too simplified to accurately predict crack initiation sites or cell wall bending.

A more accurate geometry can be obtained by “randomly” dispersing unit cells of different sizes throughout the model geometry, as was done by De Giorgi et al. [42] and Roohi et al. [19] for low- and high-density foams, respectively. However, the “random” dispersion of the cells still follows systematic algorithms, and the unit cell geometry remains highly simplified.

In order to obtain genuine randomness, a micro-CT based “voxel” model could be used. From a thermal standpoint, it has already been shown that the voxel model can yield good results [21]. Figure 17 demonstrates that the voxel model can also be

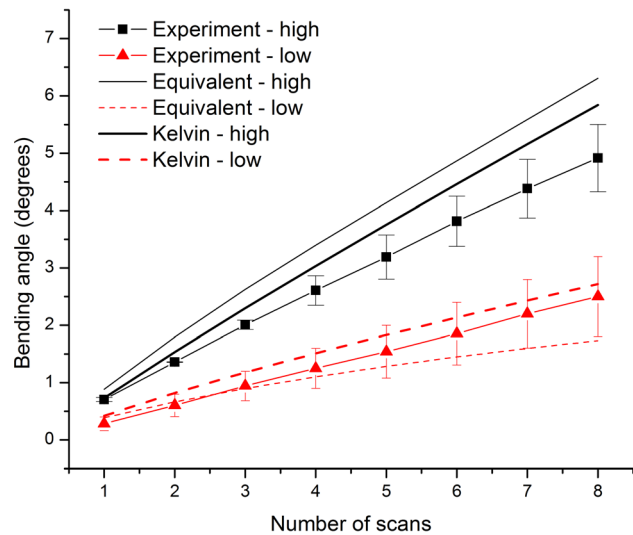
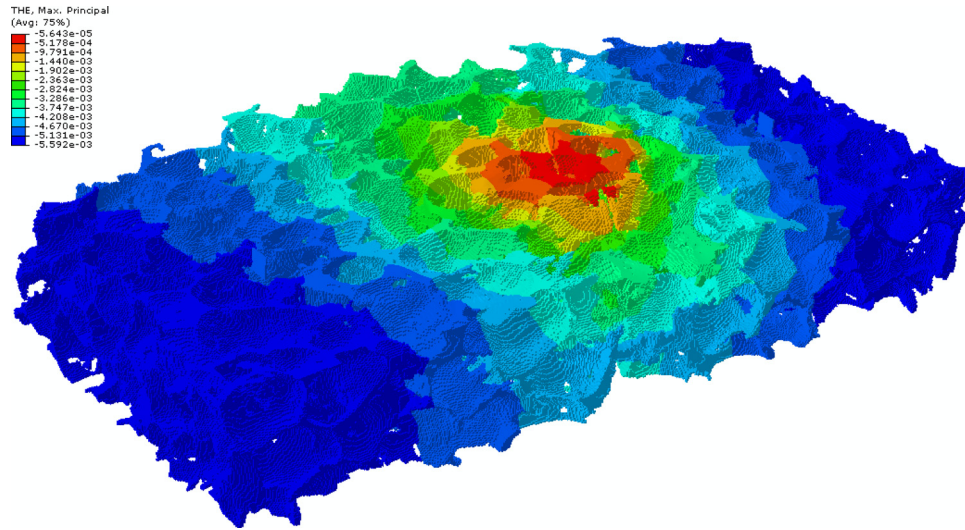


Fig. 16 Bending angles predicted by the Kelvin model in comparison with the predictions of the equivalent model and the experimental values. Standard errors are shown for the experimental data. Due to its superior geometrical accuracy, the Kelvin model yielded results that were closer to the experimental results. Nevertheless, the model still overestimated the bending angle, particularly at the high condition (180 W, 10 mm/s), since it did not account for melting, as well as changes in the laser absorption (due to using an uncoupled modeling approach).

used to model the mechanical response of the foam, showing the thermal strain distribution during a laser scan at 90 W and 5 mm/s. Due to its geometrical accuracy, particularly its capacity to model even thin cell walls, the voxel model could potentially be used to predict early-stage cracking and cell wall bending.

Despite these advantages, it is often not worth going to the great lengths of using a voxel model, since the modeling technique comes along with several disadvantages. First, each voxel model represents only one particular metal foam specimen, and it becomes necessary to generate a new voxel model for each specimen if a high level of accuracy is desired. Second, due to its extremely large number of elements, the CPU intensity increases dramatically, and the specimen size that can be modeled is limited. Due to these significant drawbacks, the equivalent and Kelvin models are in most cases adequate to model the metal foam response during laser forming, despite their limited geometrical accuracy.



**Fig. 17 Thermal strain distribution in a micro-CT based "voxel" model during a laser scan at 90 W and 5 mm/s. The downward deformation represents the initial counter-bending that occurs during the laser scan. The voxel model has a higher level of geometrical accuracy, which could potentially be used to predict crack-initiation sites and cell wall bending.**

## 5 Conclusions

In this study, the mechanical response of metal foam during laser forming was investigated. Metal foam was found to undergo compressive shortening via cell wall bending and cell crushing near the irradiated surface, as opposed to compressive plastic strains that occur in laser forming of solid sheet metal. Based on this deviation from the traditional TGM, a MTGM was proposed. From bending angle and strain measurements (determined via DIC), it was found that the achievable bending angle is limited, which can be attributed mostly to densification-induced changes in the thermal conductivity, material stiffness, flow stress, and moment of area. At bending angles around 45 deg, crack formation and cell crushing were observed. It was shown, however, that these cracks do not negatively impact the structural integrity of the foam, and the extent of the cell crushing has a minor impact on the foam crushability, since the foam remains far away from full densification and the densification is localized.

Numerically, the mechanical response of metal foam was modeled using an equivalent model, which captured the experimental trends despite using a highly simplified geometry. Alternative modeling approaches using different explicit foam geometries were discussed.

## Acknowledgment

The authors are grateful to Professor J. W. Kysar and Bob Stark for providing us with the DIC equipment and software.

## Funding Data

- National Science Foundation (Grant No. CMMI-1725980).
- Extreme Science and Engineering Discovery Environment (XSEDE) Stampede through allocation TG-DDM160002, which is supported by National Science Foundation (Grant No. ACI-1548562).

## References

- [1] Gibson, L. J., and Ashby, M. F., 1988, *Cellular Solids: Structure & Properties*, Pergamon Press, Oxford, UK.
- [2] Hebsur, M., Noebe, R., and Revilock, D., 2003, "Impact Resistance of Lightweight Hybrid Structures for Gas Turbine Engine Fan Containment Applications," *J. Mater. Eng. Perform.*, **12**(4), pp. 470–479.

- [3] Ashby, M. F., Evans, A. G., Fleck, N. A., Gibson, L. J., Hutchinson, J. W., and Wadley, H. N. G., 2000, *Metal Foams: A Design Guide*, Butterworth-Heinemann, Washington, DC.
- [4] Öchsner, A., Murch, G. E., and De Lemos, M. J. S., 2008, *Thermal Properties Simulation and Prediction*, Wiley-VCH, Weinheim, Germany.
- [5] Banhart, J., 2003, "Aluminum Foams: On the Road to Real Applications," *MRS Bull.*, **28**(4), pp. 290–295.
- [6] Banhart, J., and Seeliger, H. W., 2008, "Aluminium Foam Sandwich Panels: Manufacture, Metallurgy and Applications," *Adv. Eng. Mater.*, **10**(9), pp. 793–802.
- [7] Kennedy, A., 2012, *Powder Metallurgy, Porous Metals and Metal Foams Made From Powders*, InTech, Rijeka, Croatia, Chap. 2.
- [8] Claar, T. D., Yu, C. J., Hall, I., Banhart, J., Baumeister, J., and Seeliger, W., 2000, "Ultra-Lightweight Aluminum Foam Materials for Automotive Applications," *SAE Paper No. 2000-01-0335*.
- [9] Zu, G. Y., Lu, R. H., Li, X. B., Zhong, Z. Y., Ma, X. J., Han, M. B., and Yao, G. C., 2013, "Three-Point Bending Behavior of Aluminum Foam Sandwich With Steel Panel," *Trans. Nonfer. Met. Soc. China*, **23**(9), pp. 2491–2495.
- [10] Mata, H., Santos, A., Parente, M., Valente, R., Fernandes, A., and Jorge, N., 2014, "Study on the Forming of Sandwich Shells With Closed-Cell Foam Cores," *Int. J. Mater. Form.*, **7**(4), pp. 413–424.
- [11] Li, W., and Yao, Y. L., 2000, "Numerical and Experimental Study of Strain Rate Effects in Laser Forming," *ASME J. Manuf. Sci. Eng.*, **122**(3), pp. 445–451.
- [12] Cheng, J., and Yao, Y. L., 2004, "Process Synthesis of Laser Forming by Genetic Algorithms," *Int. J. Mach. Tool. Manuf.*, **44**(15), pp. 1619–1628.
- [13] Quadrini, F., Guglielmotti, A., Squeo, E. A., and Tagliaferri, V., 2010, "Laser Forming of Open-Cell Aluminium Foams," *J. Mater. Process. Technol.*, **210**(11), pp. 1517–1522.
- [14] Zhang, M., Chen, C. J., Brandal, G., Bian, D., and Yao, Y. L., 2015, "Experimental and Numerical Investigation of Laser Forming of Closed-Cell Aluminum Foam," *ASME J. Manuf. Sci. Eng.*, **138**(2), p. 021006.
- [15] Guglielmotti, A., Quadrini, F., Squeo, E. A., and Tagliaferri, V., 2009, "Laser Bending of Aluminum Foam Sandwich Panels," *Adv. Eng. Mater.*, **11**(11), pp. 902–906.
- [16] Santo, L., Bellisario, D., Rovatti, L., and Quadrini, F., 2012, "Microstructural Modification of Laser-Bent Open-Cell Aluminum Foams," *Key Eng. Mater.*, **504–506**, pp. 1213–1218.
- [17] Quadrini, F., Bellisario, D., Ferrari, D., Santo, L., and Santarsiero, A., 2014, "Numerical Simulation of Laser Forming of Aluminum Sponges: Effect of Temperature and Heat Treatments," *Key Eng. Mater.*, **611–612**, pp. 731–738.
- [18] Santo, L., Guglielmotti, A., and Quadrini, F., 2010, "Formability of Open-Cell Aluminium Foams by Laser," *ASME Paper No. MSEC2010-34282*.
- [19] Roohi, A. H., Naeini, H. M., Gollo, M. H., Soltanpour, M., and Abbaszadeh, M., 2015, "On the Randombased Closed-Cell Metal Foam Modeling and Its Behavior in Laser Forming Process," *Opt. Laser Technol.*, **72**, pp. 53–64.
- [20] Vollertsen, F., 1993, "The Mechanisms of Laser Forming," *CIRP Ann.*, **42**(1), pp. 301–304.
- [21] Bucher, T., Bolger, C., Zhang, M., Chen, C., and Yao, Y. L., 2016, "Effect of Geometrical Modeling on Prediction of Laser-Induced Heat Transfer in Metal Foam," *ASME J. Manuf. Sci. Eng.*, **138**(12), p. 121008.
- [22] Haijun, Y., 2007, "Research on Acoustic, Mechanical and Other Properties of Closed-Cell Aluminum Foam," Ph.D. thesis, Northeastern University, Shenyang, Liaoning, China.

- [23] Deshpande, V., and Fleck, N., 2000, "Isotropic Constitutive Models for Metallic Foams," *J. Mech. Phys. Solids*, **48**(6–7), pp. 1253–1283.
- [24] Reyes, A., Hopperstad, O. S., Berstad, T., Hanssen, A. G., and Langseth, M., 2003, "Constitutive Modeling of Aluminum Foam Including Fracture and Statistical Variation of Density," *Eur. J. Mech. A. Solids*, **22**(6), pp. 815–835.
- [25] Contorno, D., Filice, L., Fratini, L., and Micari, F., 2006, "Forming of Aluminum Foam Sandwich Panels: Numerical Simulations and Experimental Tests," *J. Mater. Process. Technol.*, **177**(1–3), pp. 364–367.
- [26] Towns, J., Cockerill, T., Dahan, M., Foster, I., Gauthier, K., Grimshaw, A., Hazlewood, V., Lathrop, S., Lifka, D., Peterson, G. D., Roskies, R., Scott, J. R., and Wilkins-Diehr, N., 2014, "XSEDE: Accelerating Scientific Discovery," *Comput. Sci. Eng.*, **16**(5), pp. 62–74.
- [27] Spittel, T., Spittel, M., and Warlimont, H., 2011, *Non-Ferrous Alloys—Light Metals*, Vol. 2C2, Springer, Berlin.
- [28] Nikanorov, S. P., Volkov, M. P., Gurin, V. N., Burenkov, Y. A., Derkachenko, L. I., Kardashev, B. K., Regel, L. I., and Wilcox, W. R., 2005, "Structural and Mechanical Properties of Al–Si Alloys Obtained by Fast Cooling of a Levitated Melt," *Mater. Sci. Eng., A*, **390**(1–2), pp. 63–69.
- [29] Mondal, D. P., Ramakrishnan, N., Suresh, K. S., and Das, S., 2007, "On the Moduli of Closed-Cell Aluminum Foam," *Scr. Mater.*, **57**(10), pp. 929–932.
- [30] Brandal, G., and Yao, Y. L., 2016, "Dislocation Generation and Cell Formation as a Mechanism for Stress Corrosion Cracking Mitigation," 35th International Congress on Applications of Lasers and Electro-Optics (ICALEO'16), San Diego, CA, Oct. 16–20.
- [31] Li, W., and Yao, Y. L., 2001, "Laser Forming With Constant Line Energy," *Int. J. Adv. Manuf. Technol.*, **17**(3), pp. 196–203.
- [32] Bastawros, A., Bart-Smith, H., and Evans, A. G., 2000, "Experimental Analysis of Deformation Mechanisms in a Closed-Cell Aluminum Alloy Foam," *J. Mech. Phys. Solids*, **48**(2), pp. 301–322.
- [33] Sutton, M. A., Orteu, J. J., and Schreier, H. W., 2009, *Image Correlation for Shape, Motion and Deformation Measurements: Basic Concepts, Theory and Applications*, Springer, New York.
- [34] Sutton, M. A., Yan, J. H., Tiwari, V., Schreier, H. W., and Orteu, J. J., 2008, "The Effect of Out-of-Plane Motion on 2D and 3D Digital Image Correlation Measurements," *Opt. Lasers Eng.*, **46**(10), pp. 746–757.
- [35] Bucher, T., Young, A., Zhang, M., Chen, C., and Yao, Y. L., 2017, "Bending Mechanism Analysis for Laser Forming of Metal Foam," *ASME Paper No. MSEC2017-3026*.
- [36] Edwardson, S. P., Abed, E., Bartkowiak, K., Dearden, G., and Watkins, K. G., 2006, "Geometrical Influences on Multi-Pass Laser Forming," *J. Phys. D: Appl. Phys.*, **39**(2), pp. 382–389.
- [37] Cheng, P., Fan, Y., Zhang, J., Yao, Y. L., Mika, D. P., Zhang, W., Graham, M., Marte, J., and Jones, M., 2006, "Laser Forming of Varying Thickness Plate—Part I: Process Analysis," *ASME J. Manuf. Sci. Eng.*, **128**(3), pp. 634–641.
- [38] Sugimura, Y., Meyer, J., He, M. Y., Bart-Smith, H., Grenstedt, J., and Evans, A. G., 1997, "On the Mechanical Performance of Closed Cell Al Alloy Foams," *Acta Mater.*, **45**(12), pp. 5245–5259.
- [39] McCullough, K. Y. G., Fleck, N. A., and Ashby, M. F., 1999, "Toughness of Aluminium Alloy Foams," *Acta Mater.*, **47**(8), pp. 2331–2343.
- [40] Janssen, M., Zuidema, J., and Wanhill, R. J. H., 2004, *Fracture Mechanics*, DUP Blue Print, London.
- [41] Blauel, J. G., 1985, "Ductile Fracture Material Characterization by J-R Curves," *Fourth Advanced Seminar on Fracture Mechanics*, Ispra, Italy, Oct. 24–28, pp. 117–143.
- [42] De Giorgi, M., Carofalo, A., Dattoma, V., Nobile, R., and Palano, F., 2010, "Aluminium Foams Structural Modelling," *Comput. Struct.*, **88**(1–2), pp. 25–35.